Short-range cation and spin ordering in the relaxor ferromagnet $La_3Ni_2SbO_9$ studied by polarized-neutron scattering and Monte-Carlo methods

Chun-Mann Chin[1], Peter D. Battle[1,*], Andrew L. Goodwin[1] and Andrew Wildes[2]

1. Inorganic Chemistry Laboratory, Oxford University, South Parks Road, Oxford, OX1 3QR, U. K.

2. Institut Laue-Langevin, BP156, 71 avenue des Martyrs, 38000 Grenoble, France

* Corresponding author: peter.battle@chem.ox.ac.uk

Abstract

Spin-polarised neutron scattering experiments have facilitated the separation of the nuclear and magnetic diffuse scattering from the partially-ordered cation distribution in the perovskite $La_3Ni_2SbO_9$. The nuclear component of the data collected at 110 and 175 K could be modelled using Monte-Carlo methods when it was assumed that the distribution of Ni^{2+} and Sb^{5+} cations over their shared six-coordinate site is that which minimises the repulsive interactions between Sb^{5+} cations ~5.5 Å apart. Analysis of the diffuse magnetic scattering showed that nearest-neighbour and next-nearest neighbour spins show short-range antiferromagnetic and ferromagnetic coupling, respectively, at 110 K. The former persists to 175 K but the latter weakens with increasing temperature.

Introduction

$La_3Ni_2SbO_9$ was first described by Alvarez *et al* as an orthorhombic perovskite with a random distribution of Ni^{2+} and Sb^{5+} over the octahedral B sites (space group: *Pbmn*) [1]. They concluded that spin canting was responsible for the ferromagnetic component observed in their magnetic susceptibility measurements, despite the fact that antiferromagnetic interactions are expected to dominate within the crystal structure. However, recent studies have revealed that the Ni^{2+} and Sb^{5+} cations are ordered in a rock–salt arrangement and the structure was assigned to the monoclinic space group $P2_1/n$ [2-4]. In this structure, the single B site in *Pbmn* is split into two inequivalent sites, one of which is fully occupied by Ni^{2+}, within error, and the other by a random distribution of Ni^{2+} and Sb^{5+} cations in a 1:2 ratio, see Figure 1.

The magnetic properties of $La_3Ni_2SbO_9$ were studied in detail by ac and dc magnetometry [2]. The magnetic susceptibility increases markedly below 105 K and the data collected under ZFC

and FC conditions differ at low temperatures. The effective magnetic moment per Ni^{2+}

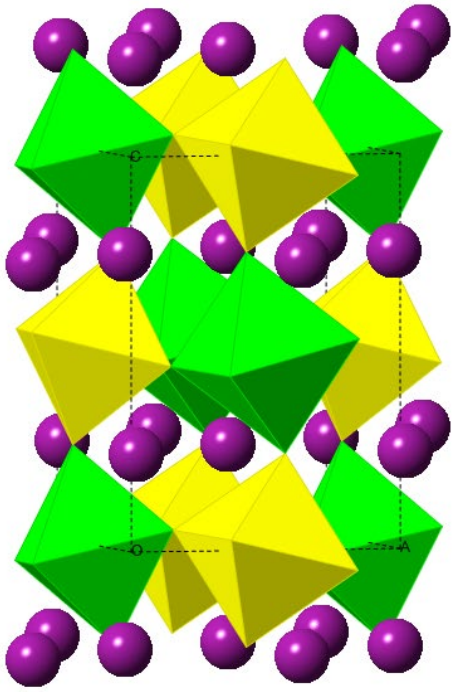

Figure 1. Crystal structure of $La_3Ni_2SbO_9$; green octahedra are occupied by Ni^{2+} cations and yellow octahedra by Ni^{2+} and Sb^{5+} cations in a 1:2 ratio. Purple spheres represent La^{3+} cations.

cation and the Weiss temperature deduced from fitting the high-temperature data to the Curie–Weiss Law were reported to be 2.2(1) μ_B and +159 K, respectively. $M(H)$ was measured at 5 K in an applied field of $-50 \leq H/\text{kOe} \leq +50$ and a magnetisation of approximately 1.5 μ_B per formula unit was measured in a field of 40 kOe. The ac susceptibility is complex below the magnetic transition temperature, which is independent of the frequency of the oscillating magnetic field. It was proposed that, even though the dominant nearest–neighbour superexchange interaction is antiferromagnetic in nature, the fact that one of the octahedral sites is fully occupied by Ni^{2+} whereas the other is only 33 % occupied by Ni^{2+} creates an imbalance of spins aligning anti–parallel to each other, leading to the formation of a ferrimagnet. However, any magnetic Bragg scattering was too weak to be observable in a neutron diffraction pattern recorded in the absence of an applied magnetic field at 5 K. This

suggests that the antiferromagnetic interaction is short–range despite the presence of structural ordering between the Ni^{2+} and the Sb^{5+} cations. A later study showed that the intensity of the magnetic Bragg peak increases with increasing strength of an applied magnetic field [5]. In contrast to the earlier work, this study did detect very weak Bragg scattering in the absence of an applied field. The local structure was examined using transmission electron microscopy [5], which revealed the presence of Sb–rich regions within the crystal structure, even though there must be strong electrostatic repulsions between these pentavalent cations. It was proposed that these compositionally-unusual regions act as domain walls which in turn disrupt the antiferromagnetic coupling between the Ni^{2+} cations as the concentration of nearest–neighbour Ni^{2+} cations is diluted. The next–nearest–neighbour magnetic interaction, and perhaps even the third–nearest–neighbour coupling, can then become more influential. The competition among these interactions causes local spin frustration and long–range magnetic ordering is only detectable when the net magnetic moments in each domain are aligned parallel by an applied magnetic field. Otherwise, the majority of the magnetic domains are too small to be detected in a neutron diffraction experiment. $Pb_3MgNb_2O_9$ (PMN), which is structurally similar to $La_3Ni_2SbO_9$, has been shown to contain nano–polar regions [6] which give rise to a net electric polarisation in the presence of an electric field. The structural distortion that gives rise to the ferroelectric properties of PMN occurs in small domains that do not give rise to Bragg peaks in an X–ray diffraction pattern [7] but the polarisations of these domains are aligned by an external electric field. The parallels between the relaxor ferroelectric PMN and $La_3Ni_2SbO_9$ led [2, 5] to the latter being described as a “relaxor ferromagnet”.

Local deviations from the average crystal structure can also be investigated by analysing the diffuse scattering embedded in a diffraction pattern. In contrast to the sharp Bragg peaks that define the average structure, features in the diffuse scattering are usually broad and weak; consequently they are often treated as background scattering. However, analysis of this

scattering can elucidate the short–range structural ordering present in a material and, if a polarised neutron beam is used, short–range magnetic ordering can also be studied. Computational models can be constructed to simulate both the structural and magnetic scattering in order to elucidate the short–range order. In this paper we describe a study of $La_3Ni_2SbO_9$ carried out using this methodology.

Experimental

Approximately 5 g of polycrystalline $La_3Ni_2SbO_9$ were synthesised by the ceramic method described previously by Battle *et al* [2] from a stoichiometric mixture of Sb_2O_5, NiO and pre–dried La_2O_3. The powder mixture was pelletised and heated at 1250 °C for nine days with intermediate grinding. The X-ray powder diffraction pattern, the dc molar susceptibility and the field dependence of the magnetisation of the product were measured to ensure that the properties of this sample were consistent with those of the sample studied previously.

Polarised neutron scattering data were collected at 110 K, slightly above the magnetic transition temperature, over the Q range $0 \leq Q/\text{Å}^{-1} \leq 2.5$ using the D7 diffractometer [8] at ILL, Grenoble with the sample mounted in an annular aluminium can. A wavelength of 4.853 Å was selected. Preliminary measurements were performed in order to facilitate the correction of the data for scattering from the sample container and for imperfect polarization. In order to separate the structural and the magnetic contributions to the total neutron scattering pattern an *xyz*–polarisation measurement [9] was conducted at each Q value measured. The experiment was repeated at 175 K, well above the magnetic transition temperature identified by magnetometry.

Results

The X-ray powder diffraction pattern of the polycrystalline sample could be modelled using a monoclinic crystal structure in the space group $P2_1/n$ with the Ni^{2+} and Sb^{5+} cations ordered in the manner described above. The refined unit cell parameters were a = 5.6037(1) Å, b = 5.6336(1) Å, c = 7.9326(1) Å, β = 90.01(1)° and V = 250.422(8) Å^3. These values are in good agreement with those published by Battle *et al*. Minimal quantities of NiO (0.20(6) wt. %) [10] and La_3SbO_7 (0.55(5) wt. %) [11] impurities were found in the reaction product. The temperature dependence of the magnetic susceptibility and the field dependence of the magnetisation of the sample were consistent with the data published previously [2].

(i) Structural short-range order at 110 K

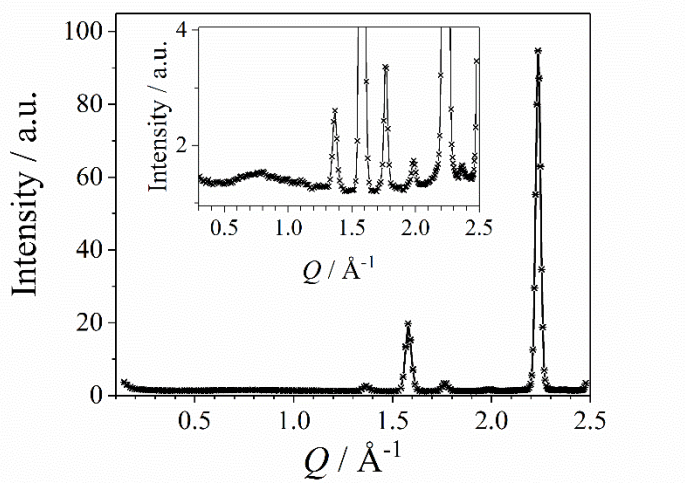

Figure 2. Nuclear coherent and isotopic incoherent scattering from $La_3Ni_2SbO_9$ at 110 K. Information regarding short–range structural order in the sample is embedded in the broad peak observed at $0.5 \leq Q/Å^{-1} \leq 1.3$, see inset.

The structural and magnetic components of the diffraction pattern were analysed separately. Figure 2 shows the nuclear coherent and isotopic incoherent scattering, which are inseparable when the *xyz* method is used [9]. As a result of the presence of two impurity phases, all intensity data in this paper are presented in arbitrary units rather than in absolute units. With the exception of the reflection at Q ~2.0 Å^{-1}, which stems from the La_3SbO_7 impurity [11], the

Bragg peaks could all be accounted for by the structural model derived previously [2]. Diffuse scattering is clearly present in the range $0.5 \leq Q/\text{Å}^{-1} \leq 1.3$, and, given that the La^{3+} and O^{2-} ions are well-ordered, it is expected to derive from short–range ordering of the Ni/Sb cations over the six–coordinate site that they occupy in a 1:2 ratio. In order to determine the details of the short–range ordering, a model which reproduces the observed scattering was generated using a Monte–Carlo (MC) approach. A cubic perovskite supercell with a chosen number of octahedral sites along each cell edge was set up as the structural template for direct Monte–Carlo (DMC) simulations. The ratio of the total number of Ni^{2+} cations to Sb^{5+} cations was fixed at 2:1 in order to be consistent with the chemical composition of $La_3Ni_2SbO_9$. The La^{3+} and O^{2-} sub-lattices were not included at this stage in the analysis. Alternate sites along the three cube axes were constrained to be occupied by Ni^{2+} cations. This represents the fact that there is a 100 % chance, within statistical error, of having a Ni^{2+} cation at the 2*c* site in $La_3Ni_2SbO_9$. Then the remaining Ni^{2+} and Sb^{5+} cations were distributed over the remaining sites (2*d*) of the supercell in a random fashion. Once the initial model was set up, the initial energy E_0 was calculated. This was done by assigning Sb^{5+} and Ni^{2+} cations to Ising states $e = +1$ and $e = -1$, respectively. The energy of the system was then taken to be summation of the product of all the next–nearest–neighbour pairs:

$$E = J \sum_{i>j}^{n} e_i e_j \qquad \text{Equation 1}$$

Here, e_i and e_j represent the states of the ions at the sites *i* and *j* respectively, and $J > 0$ represents the energy penalty associated with placing like ions on neighbouring sites of the 2*d* sublattice. Repeating pairs were ignored to avoid double calculation of the energy. It was thus assumed that the energy of the supercell was dominated by the interactions between pairs of highly-charged Sb^{5+} cations on neighboring 2*d* sites, which have a separation of $\sqrt{2}a_p$, where a_p is the unit cell parameter of a primitive cubic perovskite. The energy was minimised by calculating

the total energy of the supercell, E_1, whenever a random Sb^{5+} cation on a 2*d* site was chosen to swap with a Ni^{2+} cation on a different 2*d* site. The modified structure was accepted if E_1 was lower than E_0. Otherwise, a number was randomly generated and treated as a probability. The destabilising exchange of Ni/Sb cations was only accepted when this number was less than $\exp[-(E_1-E_0)/k_BT]$, where T is the temperature in the DMC simulations. This process was repeated until the MC loop had reached equilibrium. At this stage the La^{3+} and O^{2-} ions were added to the model and a diffraction pattern was calculated using the program CrystalDiffract®. This whole process was repeated to give a total of ten independently–generated cation configurations. The ten diffraction patterns generated were then normalised against the data collected. The same empirical, Q–dependent background function, see Figure 3, was inserted in each case and the diffraction pattern of La_3SbO_7 was also included; no Bragg peaks characteristic of NiO were observed.

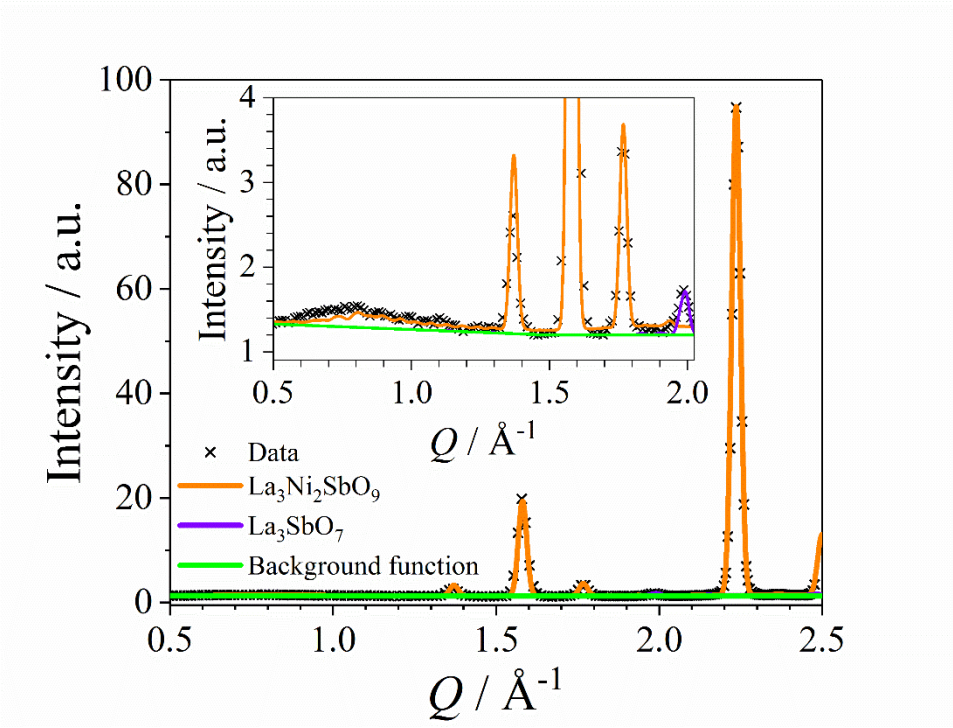

Figure 3. Simulated nuclear diffraction pattern for supercells of $La_3Ni_2SbO_9$. The orange and violet curves represent the averaged diffraction pattern of 10 independent supercells of $La_3Ni_2SbO_9$ and that of La_3SbO_7, respectively. A simple variable background function (green) has been included in the simulated diffraction pattern.

This process was repeated using a 20 x 20 x 20 supercell for a range of simulation temperatures. Preliminary calculations showed that a supercell of this size allowed the data to be well-modelled in a reasonable time; smaller cells did not result in a good fit and the use of larger cells would have increased the computation time. The best fit to the data was obtained for $k_BT/J = 0.53$. The average of the nuclear diffuse scattering patterns calculated in this way from 10 independent nuclear configurations is compared to the observed data in Figure 3; the empirical background function is also shown. In our analysis we are thus modelling the diffuse scattering as Bragg scattering from the long d-spacing reflections of a large supercell. Note that this model does not take into account any additional contribution to the nuclear scattering arising from correlated structural relaxation driven by cation order. This is why the intensity of the diffuse feature is slightly underestimated, even if its width and position are well accounted for.

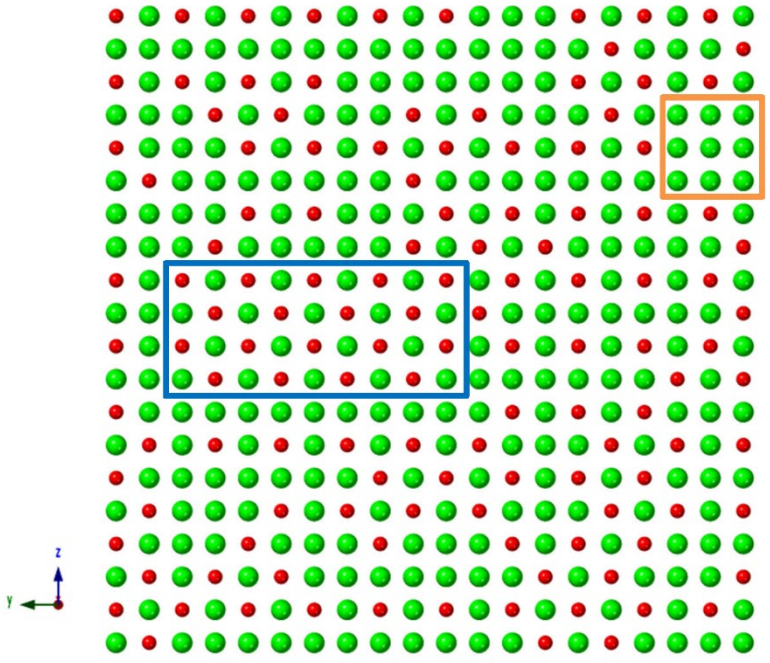

Figure 4. [100] slice of the 20 x 20 x 20 supercell ($0.3 \leq x \leq 0.35$, $0 \leq y \leq 1$, $0 \leq z < 1$) of $La_3Ni_2SbO_9$ showing the Ni/Sb distribution generated by a DMC simulation. The green and red spheres represent Ni^{2+} and Sb^{5+} cations, respectively. The blue rectangle indicates a region wherein 5.5 Å Sb–Sb contacts are retained whereas the orange square shows a Ni^{2+} cluster which compensates for the existence of the Sb–rich region.

Figure 4 shows the cation distribution in a slice of one of the ten configurations generated in the calculations. There are regions showing hints of a checkerboard arrangement of Ni/Sb in this supercell, see the blue rectangle in Figure 4. This does not represent a failure of the energy constraint set in the DMC calculations because there is no way to arrange the cations so as to completely avoid Sb/Sb next–nearest–neighbour pairs and, furthermore, the simulation was performed at a finite temperature so violations must be allowed. These regions are compensated for by regions which can be considered to be Ni clusters, see the orange square in Figure 4.

A site correlation function

$$g(r) = \frac{1}{Z(r)} \sum_{\langle i,j \rangle_r} e_i e_j \qquad \text{Equation 2}$$

was calculated and the normalised variant $g'(r) = \frac{9}{8}\left[g(r) - \frac{1}{8}\right]$ is shown in Figure 5. This function renormalises $g(r)$ as appropriate for this stoichiometry. Here the sum is taken over Sb/Ni site pairs i,j separated by distance r, with $Z(r)$ the total number of such pairs for given r. Fitting an exponential envelope to this function resulted in a correlation length $\xi = 5.3$ Å.

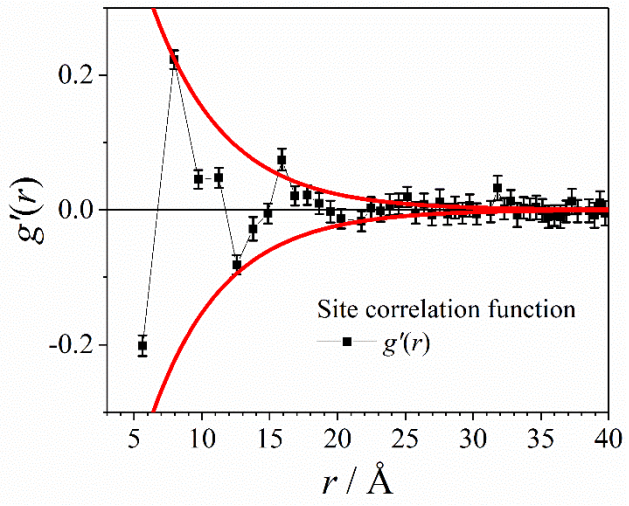

Figure 5. The site correlation function of a particular nuclear configuration of a supercell of $La_3Ni_2SbO_9$ after a DMC simulation. The red curve is a fitted exponential envelope.

(ii) Magnetic short-range order at 110 K

The magnetic scattering from $La_3Ni_2SbO_9$ at 110 K, after appropriate initial processing and binning, is shown in Figure 6. A broad peak can be seen where $1.0 \leq Q/\text{Å}^{-1} \leq 1.7$; this peak lies under a non–magnetic Bragg peak when the experiment is performed using unpolarised neutrons. No magnetic scattering from the NiO impurity was detected. Both DMC and reverse Monte–Carlo (RMC) approaches were then used to deduce the spin configuration of the paramagnetic Ni^{2+} cations.

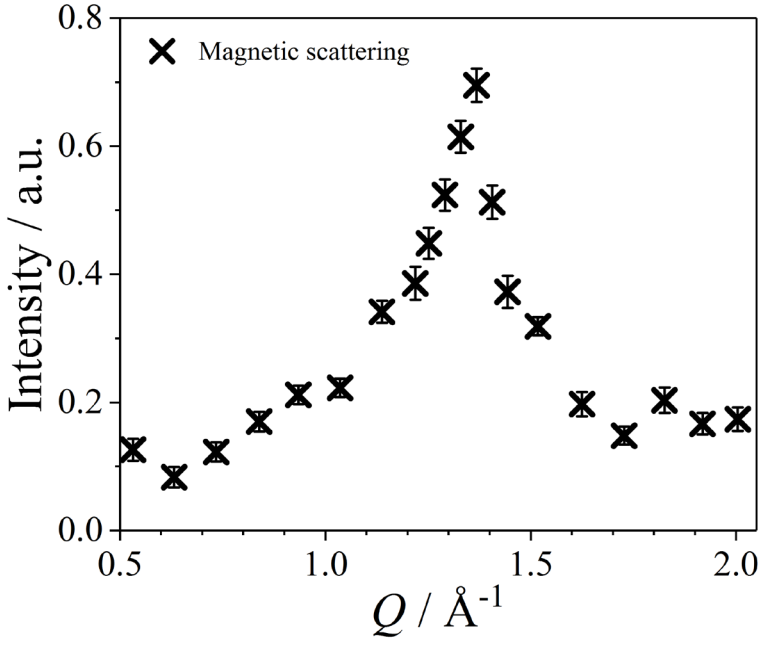

Figure 6. Magnetic scattering from $La_3Ni_2SbO_9$ at 110 K

(a) The RMC approach

The magnetic diffuse scattering was initially analysed using the SPINVERT package [12] which implements a RMC algorithm [13]. A supercell of 20×20×20 octahedral sites was populated according to the cation distribution shown in Figure 4. However, Sb^{5+} is diamagnetic and so only the paramagnetic S = 1 Ni^{2+} cations, and hence a total of 5334 spin vectors, were present in this cell. Each Ni^{2+} cation was assigned a random spin orientation and the

corresponding scattering pattern was calculated. The sum of squared residuals, χ_{RMC}^2, was calculated as follows:

$$\chi_{RMC}^2 = W \sum_Q \left[\frac{sI_{calc}(Q) - I_{expt}(Q)}{\sigma(Q)}\right]^2 \qquad \text{Equation 3}$$

where $I_{calc}(Q)$ and $I_{expt}(Q)$ represent the calculated and experimental values of powder–averaged magnetic scattering intensity, $\sigma(Q)$ is an experimental uncertainty, W is an empirical weighting factor and s is a refined overall scale factor. The spin vector of a randomly-chosen Ni^{2+} cation was then allowed to rotate by a small amount. This proposed move was either accepted or rejected according to the METROPOLIS algorithm [14]. This process was repeated until no further reduction in χ_{RMC}^2 was observed. The calculated magnetic diffuse scattering patterns calculated from 10 independent initial spin configurations were averaged in order to minimise the statistical noise. Calculations were performed with W = 10000 and the resulting magnetic diffuse scattering patterns are shown in Figure 7. The calculated pattern fitted both the width and the intensity of the peak.

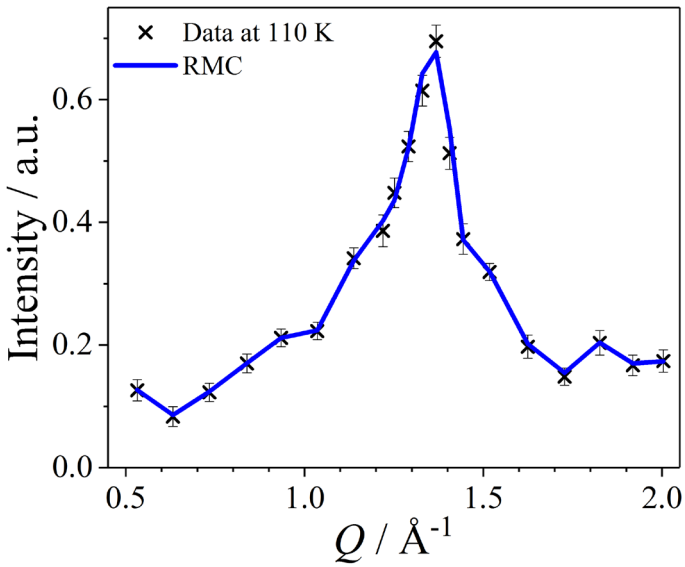

Figure 7. Observed and RMC-simulated magnetic scattering pattern from $La_3Ni_2SbO_9$ at 110 K.

(b) The DMC approach

Although the data-driven RMC calculations, with a large number of degrees of freedom, account well for the observed scattering, they give no information about the relative strengths of the magnetic coupling constants, J_n, that operate within the structure. However, this information can be deduced from the results of our DMC calculations. Simulations were performed using the same nuclear template, and hence there was again a total of 5334 spins in the supercell. A spin configuration was initialised with random spin orientations in an algorithm which subsequently cooled the sample at a rate of:

$$T_i = (0.9)^i T_0 \qquad \text{Equation 4}$$

where T_i is the temperature at the i^{th} step of the algorithm and T_0 is the initial temperature which was set to 200 K in all DMC simulations. Spins were allowed to rotate at each temperature for equilibration. If equilibrium was not reached, the simulations were terminated. After each move, the energy was calculated using Equation 5

$$E = -\frac{1}{2}\sum_n \sum_{i,j} J_n \boldsymbol{S}_i . \boldsymbol{S}_j \,, \qquad \text{Equation 5}$$

where J_n is the superexchange constant between n^{th} nearest neighbours and $\boldsymbol{S}_i$and $\boldsymbol{S}_j$ represent the spins of the n^{th} nearest neighbours at the $i^{th}$and j^{th} sites. Different ratios of the relative strength of the superexchange interactions were used in different DMC runs. The magnetic diffuse scattering was calculated, using the SPINDIFF routine in the SPINVERT package, from six independent spin configurations generated by successive DMC simulations.

Clearly the magnetic exchange constants between pairs of spins, $J_{n,}$, must be defined before a DMC simulation. Figure 8 illustrates the four shortest distances between a Ni^{2+} cation occupying a 2*c* site (bottom left corner) and other Ni^{2+} cations. J_1 is the interaction between nearest–neighbour Ni^{2+} cations and this interaction was assumed to be antiferromagnetic and

to be equal in strength to the Ni–O–Ni interactions reported for NiO by Hutchings *et al* [15]. This assumption is not perfect because the bond distances and bond angles in $La_3Ni_2SbO_9$ are slightly different from those in NiO and the acidity of the La^{3+} cations will also affect the strength of the superexchange interaction. Nevertheless, in all simulations J_1/k_B was fixed at the value of –221 K reported by Hutchings *et al*. J_3 is the interaction with the third–nearest–neighbour paramagnetic cation which is ~6.9 Å away. The distance between them is relatively long and the superexchange pathway involves at least three oxide anions. As a result, J_3 was considered to make a negligible contribution to the magnetic coupling and was given a value of zero in all DMC simulations. J_2 and J_4 are the 90° and linear Ni–O–*B*'–O–Ni superexchange interactions, respectively. They can be significant in an ordered double perovskite if the *B*' cation is diamagnetic, for example [16, 17] W^{6+} or Te^{6+}. DMC calculations were performed with a number of different values for J_2 and J_4.

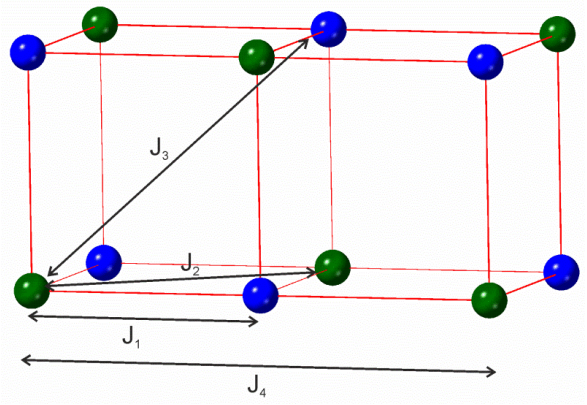

Figure 8. Superexchange pathways in $La_3Ni_2SbO_9$.. Green and blue spheres represent the Ni^{2+} cations located at the 2*c* and 2*d* sites respectively.

The values of J_2 and J_4 reported by Blasse and Iwanaga *et al* [16, 17] for the cation-ordered double perovskites Sr_2NiWO_6 and Sr_2NiTeO_6 were used initially. They, along with the value of J_1 from NiO, were applied to the selected structural model to generate three independent magnetic diffuse scattering patterns using the program SPINDIFF, see Figure 9a. Neither the

width nor the maximum intensity of the peak is well-fitted by any pair of the published J_2 and J_4 values. Despite the presence of different types of diamagnetic *B*' cations in Sr_2NiWO_6 and

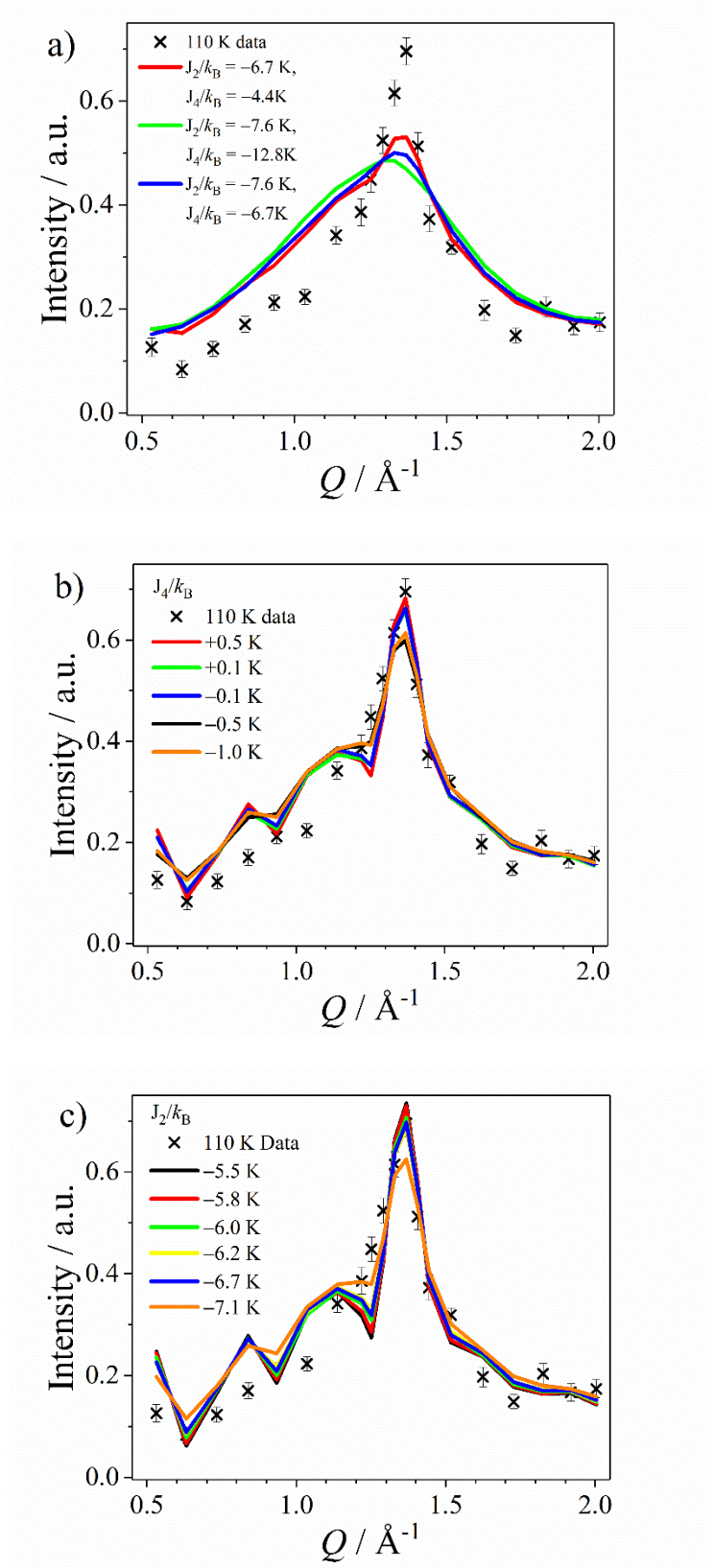

Figure 9. Observed and DMC-simulated magnetic scattering patterns of $La_3Ni_2SbO_9$ (a) generated with J_1/k_B = –221 K and published values of J_2/J_4, (b) as a function of J_4/k_B with J_1/k_B = –221 and J_2/k_B =–7.1 K and (c) as a function of J_2/k_B with J_1/k_B = –221 K.

Sr_2NiTeO_6, the J_2/k_B values reported are very similar. It was therefore decided to set J_2/k_B equal to a value intermediate between those in the literature, *i.e.* –7.1 K, and to investigate the consequences of changing the value of the J_4/k_B. The result of this modelling is shown in Figure 9b; it is apparent that $J_4/k_B \sim 0$ K when J_1/k_B = -221 K and J_2/k_B = –7.1 K, indicating that the linear superexchange interaction mediated by a diamagnetic Sb^{5+} cation has little influence on the magnetic structure adopted. Consequently, the superexchange pathways J_1 and J_2 are the only ones that need to be considered in order to account for the magnetic diffuse scattering. Further calculations were therefore carried out with J_4/k_B = 0 K, and J_2/k_B (effectively the ratio of J_1/J_2) as the only variable. The scattering was simulated using a range of J_2/k_B values and the calculated patterns, together with the observed data, are plotted in Figure 9c. The pattern generated with J_1/k_B =–221 and J_2/k_B = –6 K gives a satisfactory fit to both the width and intensity of the observed peak. This value of J_2/k_B is similar to that reported by Blasse and Iwanaga *et al* for Sr_2NiWO_6 and Sr_2NiTeO_6.

A spin correlation function, $\langle \boldsymbol{S}.\boldsymbol{S} \rangle(r)$, was calculated in order to provide an overview of the spin coupling, see Figure 10. Positive and negative values of $\langle \boldsymbol{S}.\boldsymbol{S} \rangle(r)$ correspond to ferromagnetic and antiferromagnetic coupling, respectively. For comparative purposes, the functions derived from both RMC and DMC calculations are shown in Figure 10. In each case, the oscillatory spin correlation function is characteristic of antiferromagnetic order. The RMC simulations show no long-range order, since the correlation function decays towards zero at large distances. By contrast, the DMC simulations lead to an ordered spin arrangement. This might be an indication that the magnitude of the superexchange constant in NiO is larger than the true value in $La_3Ni_2SbO_9$. The RMC approach always produces the most disordered model

which is consistent with the data. Consequently, the correlation length determined from the exponential envelope of the RMC results ($\xi \sim 9$ Å) gives a lower bound on the coherence length scale for magnetic order in $La_3Ni_2SbO_9$. Likewise the DMC calculations clearly overestimate the strength of magnetic order. This is evident in the width of the primary magnetic scattering peak, which is too small in the DMC calculations, see Figure 9. That both RMC and DMC converge on essentially the same type of local magnetic order is made clear by introducing an exponential damping factor into the DMC results. This is equivalent to convolving the reciprocal-space fit with a Lorentzian broadening function. Our best fit is then obtained for a coherence length of ξ = 12 Å, which may be a more realistic estimate of the characteristic length-scale of antiferromagnetic order in $La_3Ni_2SbO_9$.

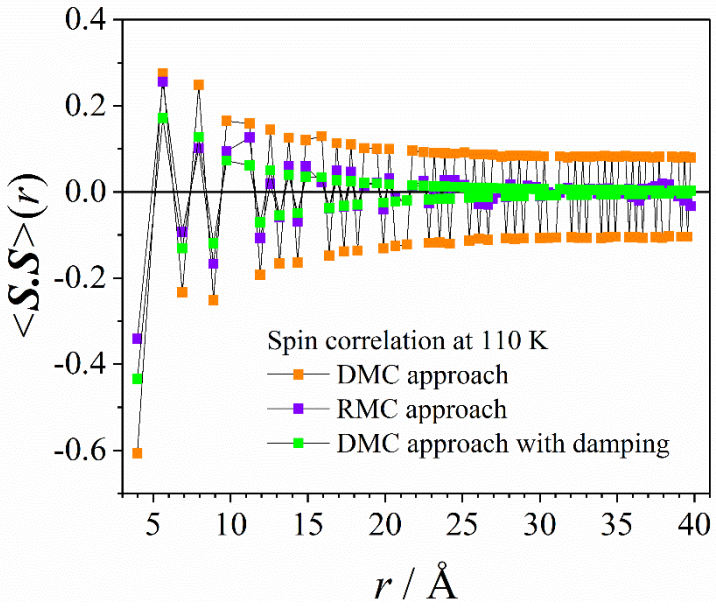

Figure 10. Spin correlation function of $La_3Ni_2SbO_9$ at 110 K as derived from the RMC and DMC models.

(iii) Structural and magnetic short-range order at 175 K

Attempts were made to analyse the corresponding data collected at 175 K using an approach similar to that described above. Figure 11 shows the nuclear and isotopic incoherent scattering recorded at 110 and 175 K. The two patterns are superimposable, as expected, and the nuclear

template established from the 110 K data was therefore used to analyse the magnetic scattering observed at 175 K.

The magnitude of the magnetic diffuse scattering was weaker at 175 K than that at 110 K, see Figure 12, demonstrating that spin fluctuations in $La_3Ni_2SbO_9$ increase as the temperature is increased.

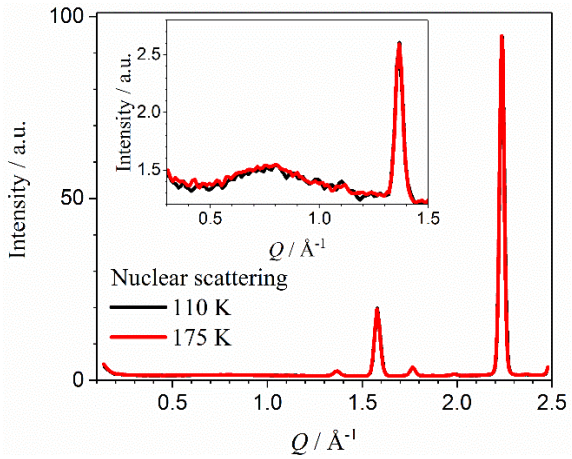

Figure 11. Nuclear coherent and isotopic incoherent scattering from $La_3Ni_2SbO_9$ at 110 K (black) and 175 K (red). The inset shows a magnification of the low Q region.

Three magnetic scattering patterns were calculated using both the DMC and RMC approaches, see Figure 13. For the former, two independent models were used; one of them included the linear Ni–O–*B*'–O–Ni superexchange pathway (J_1/k_B = –221 K, J_2/k_B = –7.1 K and J_4/k_B = –0.1 K) whereas the other used only J_1 and J_2 (J_1/k_B = –221 K and J_2/k_B = –6 K). Neither produced satisfactory fits to the data collected at 175 K, see Figure 13, implying that the ratios of the superexchange constants, J_n, deduced previously are not applicable here. The exchange constants might be a function of temperature but it is more likely that the over–estimation of J_1 discussed above has a greater effect on the fit at higher temperatures. The poor counting statistics made it impossible to obtain reliable ratios of the exchange constants at 175 K. In contrast, the data-driven RMC calculation again produced an acceptable fit to the data.

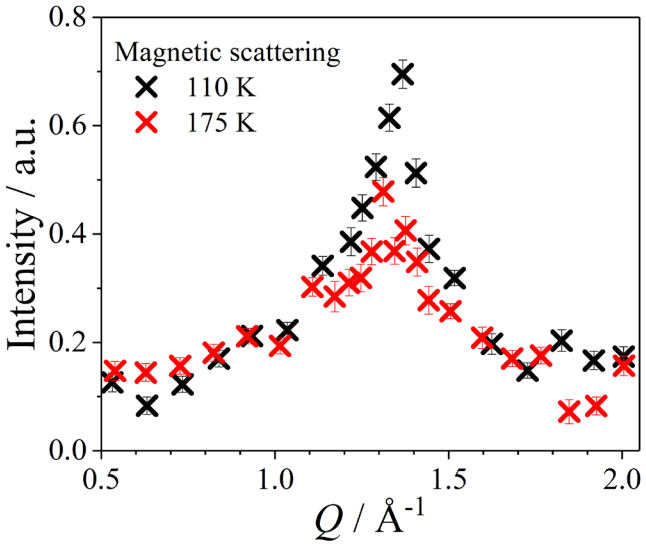

Figure 12. The average magnetic scattering patterns of $La_3Ni_2SbO_9$ at 110 K (black) and 175 K (red).

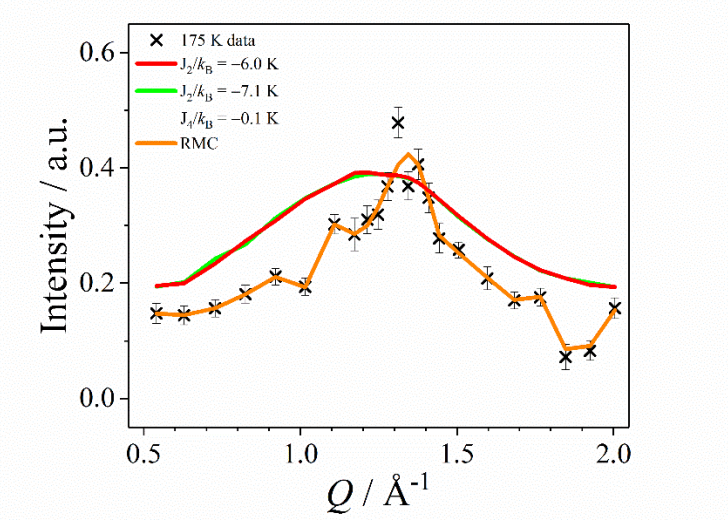

Figure 13. Fits to the magnetic scattering from $La_3Ni_2SbO_9$ at 175 K calculated using DMC (red and green curves) and RMC (orange curve) methods.

The function $\langle \boldsymbol{S}.\boldsymbol{S} \rangle(r)$ obtained from the data collected at 175 K using an RMC approach is compared to the 110 K counterpart in Figure 14. At both temperatures $\langle \boldsymbol{S}.\boldsymbol{S} \rangle(r)$ oscillates and decays towards zero when $r > 15$ Å. The value of the correlation function for the nearest–neighbour interaction ($r \sim 4$ Å) does not change between 110 K and 175 K whereas that between

next–nearest–neighbours at $r \sim 5.5$ Å clearly decreases on warming. The spin correlation length at 175 K was calculated to be 9 Å.

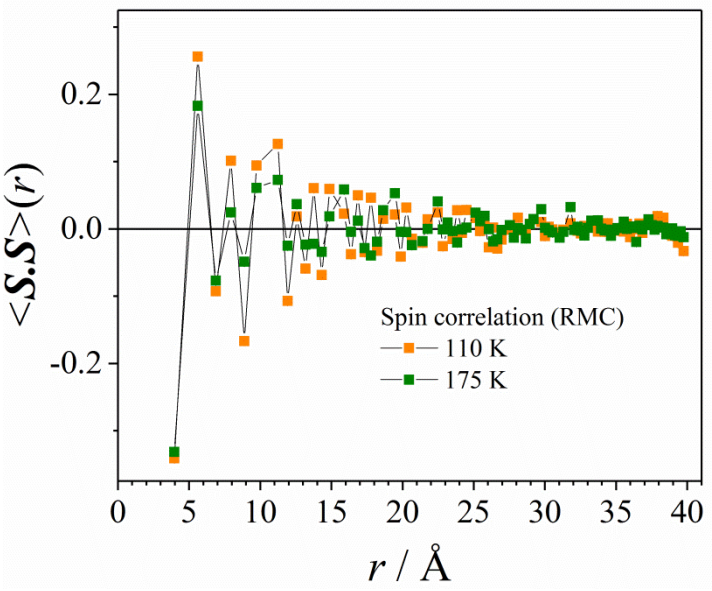

Figure 14. The spin correlation function of $La_3Ni_2SbO_9$ as a function of temperature.

Discussion

The X–ray diffraction and magnetometry data collected on the newly prepared sample of $La_3Ni_2SbO_9$ are consistent with those collected on the original sample [2] although there will certainly be some small variation in the degree of local ordering in two different samples.

The energy constraints used in the DMC calculation play a crucial role in determining the local Ni/Sb distribution which, in turn, determines the nature of the diffuse scattering. This scattering was well-modelled when a constraint describing the electrostatic next–nearest–neighbour Sb^{5+}–Sb^{5+} repulsion was the only one included in our calculations, suggesting that it is the dominant interaction. Our analysis of the nuclear diffuse scattering shows that nickel-rich regions form in order to accommodate the Sb – Sb repulsions, see Figure 4. Nearest-neighbour antiferromagnetic coupling is likely to be strong in the Ni-rich regions at temperatures well above 110 K. This is consistent with the low value of μ_{eff} reported [2] in the temperature range

$150 < T/\mathrm{K} < 300$ and also with the negligible decrease in $\langle \boldsymbol{S}.\boldsymbol{S} \rangle(r)$ for nearest neighbour cation pairs. The largest of these regions might be responsible for the weak magnetic Bragg scattering observed at 5 K in the absence of an applied field [5].

The non-random distribution of Ni^{2+} and Sb^{5+} over the 2*d* sites is consistent with the observation of variations in the cation distribution in the previous TEM experiments [5], but the nature of the variation is different. For example, the Sb-rich regions observed by microscopy in one particular crystallite of $La_3Ni_2SbO_9$ appear to extend over a distance of ~ 80 Å, whereas the diffuse scattering data suggest that the short-range order on the 2*d* sites, which gives rise to Ni-rich regions, persists over a much shorter distance. Of course the TEM experiment sampled only a small number of local regions whereas the neutron scattering experiment sampled the bulk material. It is possible to reconcile the two observations by postulating that Sb-rich regions occur in the domain boundaries to compensate for Ni-rich regions within the domains, but further experimental work would be necessary in order to prove this.

The DMC calculations have shown that the linear superexchange pathway Ni–O–*B*'–O–Ni, approximately 8 Å in length, is insignificant in $La_3Ni_2SbO_9$ at 110 K. If the *B*' cation is Sb^{5+}, there will be a mismatch in energy between the low–lying filled Sb^{5+} 4*d* orbital and 2*p* orbitals of O^{2-}, and hence the coupling will be weak [18, 19]. If the *B*' cation is Ni^{2+}, J_4 will be small compared to the strongly antiferromagnetic J_1 interaction which would then be expected to dominate. The low value found for J_2/k_B suggests that the mean next–nearest–neighbour magnetic interaction depends on the Ni/Sb distribution. If the *B*' cation is a diamagnetic Sb^{5+} cation, the coupling between the next–nearest–neighbour Ni^{2+} cation (Ni–O–O–Ni) is expected to be antiferromagnetic and J_2/k_B should then be negative. However, there is a 33 % probability that a Ni^{2+} cation will be on the *B*' site. In this case, the superexchange pathway is slightly different; it should now involve an additional Ni^{2+} cation between the two oxide anions, and

the J_2 interaction is expected to be positive, as it is in NiO [15]. As a result, the mean J_2 interaction is less strongly antiferromagnetic than might be expected. Nevertheless, further adjustment of the J_n values is clearly required as the J_2/J_1 ratio deduced from the data collected at 110 K was unable to model the magnetic data collected at 175 K. Although this might indicate that the magnetic interactions are temperature dependent, the spin correlation function derived from the RMC approach, see Figure 10, suggests that the antiferromagnetic interaction between nearest–neighbour Ni^{2+} cations may not be as strong as in the case of NiO. If so the value of J_2 used to model the magnetic diffuse scattering at 110 K will also be inaccurate. The spin correlation functions $<\boldsymbol{S}.\boldsymbol{S}>(r)$ calculated using both the DMC and RMC approaches, see Figure 10, show that the spin vectors are essentially uncorrelated beyond $r \sim 15$ Å. The magnetic correlation length is significantly longer than the value, 5.3 Å, derived to describe the persistence of cation ordering, see Figure 5. This suggests that the magnetic ordering is relatively robust against variations in the cation distribution, perhaps because of the high connectivity of the magnetic structure.

The nuclear scattering data collected at 175 K match those collected at 110 K, meaning the nuclear template is temperature independent. This is not surprising. In contrast, the diminished intensity of the magnetic scattering recorded at the higher temperature shows that the extent of short–range magnetic ordering decreases as the temperature increases. The spin correlation function shown in Figure 14 indicates the magnetic correlation length is not a function of temperature as the RMC-based $g(r)$ decays towards zero at a similar distance at both temperatures. However, the degree of spin correlation between next–nearest–neighbour cations ($r \sim 5.5$ Å) decreases with temperature faster than that between nearest neighbours. This suggests that the increase in the thermal energy gained by the spins reduces the correlation between the spins at the relatively longer distance. Further work, specifically the determination of J_1 and J_2, is required in order to advance our understanding of this complex compound.

Conclusion

Scattering experiments performed using a spin-polarised neutron beam have facilitated the separation of the nuclear and magnetic diffuse scattering from $La_3Ni_2SbO_9$. The nuclear component of the data collected at 110 and 175 K could be modelled by assuming that the distribution of Ni^{2+} and Sb^{5+} cations over their shared six-coordinate site is that which minimises the repulsive interaction between Sb^{5+} cations ~5.5 Å apart. The short-range ordering thus induced leads to the formation of both nickel-rich regions and 1:1 ordered regions. The short-range cation ordering persists over distances characterised by a correlation length of 5.3 Å. Analysis of the magnetic component of the scattering recorded at 110 K reveals the presence of relatively strong antiferromagnetic coupling between Ni^{2+} cations on nearest-neighbour sites and relatively weak ferromagnetic alignment of those on next-nearest neighbour sites; this ordering is characterised by a correlation length of ~10 Å. On warming to 175 K the latter diminishes more than the former.

Acknowledgments

CMC thanks the Croucher Foundation and Oxford University for a graduate scholarship. Data were collected at ILL in expt. no. 5-32-806; http://doi.ill.fr/10.5291/ILL-DATA.5-32-806.

References

[1] I. Alvarez, M.L. Veiga, C. Pico, Journal of Alloys and Compounds 255 (1997) 74-78.
[2] P.D. Battle, S.I. Evers, E.C. Hunter, M. Westwood, Inorg. Chem. 52 (2013) 6648- 6653.
[3] D.G. Franco, R.E. Carbonio, E.E. Kaul, G. Nieva, J. Magn. Magn. Mater. 346 (2013) 196.
[4] D.G. Franco, R.E. Carbonio, G. Nieva, IEEE Trans. Magnetics 49 (2013) 4656.
[5] P.D. Battle, M. Avdeev, J. Hadermann, J. Solid State Chem. 220 (2014) 163 - 166.
[6] A.A. Bokov, Z.G. Ye, Journal of Materials Science 41 (2006) 31-52.
[7] P.K. Davies, M.A. Akbas, Journal of Physics and Chemistry of Solids 61 (2000) 159-166.
[8] J.R. Stewart, P.P. Deen, K.H. Andersen, H. Schober, J.F. Barthelemy, J.M. Hillier, A.P. Murani, T. Hayes, B. Lindenau, Journal of Applied Crystallography 42 (2009) 69-84.
[9] O. Scharpf, H. Capellmann, Physica Status Solidi a-Applied Research 135 (1993) 359-379.
[10] G.A. Slack, Journal of Applied Physics 31 (1960) 1571-1582.
[11] K.P.F. Siqueira, R.M. Borges, E. Granado, L.M. Malard, A.M. de Paula, R.L. Moreira, E.M. Bittar, A. Dias, Journal of Solid State Chemistry 203 (2013) 326-332.

[12] J.A.M. Paddison, J.R. Stewart, A.L. Goodwin, Journal of Physics-Condensed Matter 25 (2013).
[13] R.L. McGreevy, L. Pusztai, Molecular Simulation 1 (1988) 359-367.
[14] N. Metropolis, A.W. Rosenbluth, M.N. Rosenbluth, A.H. Teller, E. Teller, Journal of Chemical Physics 21 (1953) 1087-1092.
[15] M.T. Hutchings, E.J. Samuelsen, Physical Review B-Solid State 6 (1972) 3447-3461.
[16] G. Blasse, Philips Res. Repts. 20 (1965) 327 - 336.
[17] D. Iwanaga, Y. Inaguma, M. Itoh, Mater. Res. Bull. 35 (2000) 449 - 457.
[18] V.M. Katukuri, P. Babkevich, O. Mustonen, H.C. Walker, B. Fak, S. Vasala, M. Karppinen, H.M. Ronnow, O.V. Yazyev, https://arxiv.org/abs/1902.09376 (2019).
[19] O. Mustonen, S. Vasala, K.P. Schmidt, E. Sadrollahi, H.C. Walker, I. Terasaki, F.J. Litterst, E. Baggio-Saitovitch, M. Karppinen, Physical Review B 98 (2018) 064411.